Modeling Permporometry of Mesoporous Membranes Using Dynamic Mean Field Theory

Ashutosh Rathi, John R. Edison, David M. Ford, and Peter A. Monson
Dept. of Chemical Engineering, University of Massachusetts, Amherst, MA 01003-9303

DOI 10.1002/aic.14846
Published online August 7, 2015 in Wiley Online Library (wileyonlinelibrary.com)

Mesoporous inorganic membranes have significant potential for important small-molecule separations like carbon dioxide recovery from stack emissions. However, tailoring materials for a given separation remains an outstanding problem. Preferential adsorption, layering and capillary effects, and surface flow are key mechanisms that determine permeation rates and are ultimately linked to the mesopore characteristics. To further the understanding of these systems, a modeling approach based on dynamic mean field theory, which has previously been used to study the dynamics of adsorption in mesoporous materials, is proposed. This theory describes both relaxation dynamics and nonequilibrium steady states in membranes and is fully consistent with a mean field density functional theory of the thermodynamics. The capabilities and promise of the approach by modeling a permporometry experiment, in which a light gas permeates through a mesopore in the presence of a condensable vapor at a controlled relative pressure, are demonstrated. © 2015 American Institute of Chemical Engineers *AIChE J*, 61: 2958–2967, 2015
Keywords: membrane separations, thermodynamics/statistical, diffusion (in membranes), adsorption/gas

Introduction

Mesoporous inorganic membranes have long been of interest in the separations field[1–3] due to their technologically relevant pore-size range (diameter 2–50 nm) and chemical and thermal stability. Typically, these membranes comprise of a mesoporous metal oxide (e.g., silica and alumina) layer with thickness ~0.1–10 μm, which provides the desired separation functionality, deposited on a much thicker macroporous substrate for mechanical support. In the earliest generation of materials,[4,5] the mesoporous layer was made by slipcasting colloidal suspensions of small alumina crystallites, which resulted in disordered pore structures with a relatively wide pore-size distribution (PSD). The current research frontier for synthesis of mesoporous silica films involves the use of organic molecular templates to grow highly uniform silica mesopore structures *in situ*. Self-supporting mesoporous silica thin films have been prepared at air/water interfaces.[6–8] Mesoporous silica films on flat surfaces including mica, graphite, silicon wafer, and glass substrate have been fabricated by a combination of coating techniques with self-assembly approaches.[9–12] The orientation of mesoporous silica films can be controlled, using a continuous flow of synthesis mixture parallel to the surface or additional high magnetic fields. Maintaining pore connectivity normal to the support interface and producing films that are sufficiently thin, yet mechanically stable and defect-free, are still major challenges.[2,3] However, the past 20 years have seen steady progress towards the goal of delivering a given mesoporous material in the form of a practically useful separation membrane.

Applications of mesoporous inorganic membranes are wide-ranging; they include microfiltration and ultrafiltration for water purification,[13] removal of solids in beverage manufacture,[14] and concentration of cellular organisms in fermentation processes.[15] More to the point of this article, these membranes are also potentially useful in separations involving smaller molecular species, such as carbon dioxide, alcohols, and hydrocarbons, which are important in the energy and chemical industries. Specific examples include carbon dioxide recovery from stack emissions,[16–18] volatile organic compound (VOC) recovery and recycle,[19,20] and ethanol/water separation for biofuel production.[21] Small-molecule separations with mesoporous membranes typically utilize mechanisms like preferential adsorption and surface diffusion because the mesopores are too large to perform molecular sieving. In fact, the counterintuitive result of preferential permeation of the larger, heavier molecular species is often observed. Huang et al. showed that separation factors of 10^2-10^3 for acetone (a model VOC) over nitrogen could be achieved with disordered mesoporous alumina membranes, provided that the operating conditions (temperature and partial pressure) supported capillary condensation of the acetone in the pores.[20] Pore size, and more generally pore geometry, is obviously an important material variable that can be tuned to promote desired adsorption and transport mechanisms. Surface chemistry is another such variable. Ford and coworkers previously demonstrated that functionalizing disordered alumina or ordered silica membranes with organosilanes enhanced their selectivity for small hydrocarbons over air by as much as a factor of 10, presumably by promoting adsorption and surface flow of the hydrocarbon in the pores.[22–27] Sakamoto et al.[17]

Additional Supporting Information may be found in the online version of this article.

Correspondence concerning this article should be addressed to Peter A. Monson at monson@ecs.umass.edu.

synthesized MCM-48 membranes and evaluated them for carbon dioxide recovery; the membranes in their native state exhibited a CO_2/N_2 selectivity of 0.8 (consistent with a purely Knudsen flow mechanism), but when functionalized with an aminopropylsilane the selectivity increased to 50 or more (albeit with a significant drop in overall permeance).

Mesoporous membrane separation research is at a stage where synthesis of materials with finely controlled pore structures and surface chemistries is possible, but the "design rules" for tailoring the properties to a specific separation are still unclear because of the complexities of the separation mechanisms. Availability of a permeation prediction method that combines a sufficient level of molecular detail with computational efficiency would be a major step forward in the design of mesoporous inorganic membranes for separations. Molecular modeling[28–32] provides atomistic detail but is not computationally efficient; the length of a typical pore model is only ~1% of the actual membrane thickness, and the dynamic trajectories cover only ~10 ns of real time. Continuum modeling is computationally efficient but has no atomistic detail and thus requires the transport mechanisms as input, rather than predicting them as emergent behavior. In this work, we deploy a lattice model approach that strikes a balance between molecular detail and efficiency. Our approach has its basis in the classical density functional theory (DFT) of confined fluids that has been extensively used to study the thermodynamics of fluids confined in mesoporous materials.[33–36] DFT provides a theory of both the free energy and the density distribution of confined fluids. In addition to yielding enormous theoretical insights into the behavior of these systems,[33,36] DFT has become an essential component of porous materials characterization methods based on adsorption. It is typically featured in the software that accompanies commercial adsorption measurement equipment for porous materials characterization. Although DFT is much less computationally intensive than molecular simulations, the computational effort grows substantially with dimensionality. Under these circumstances, coarse-grained lattice model approaches are finding considerable utility.[36] In modeling membrane systems, we have to consider the transport as well as the thermodynamics, as we are typically concerned with a nonequilibrium steady state with a chemical potential gradient across the membrane. To address this situation, we can employ an adaptation of DFT to the case of nonequilibrium states. We refer to this theory as dynamic mean field theory (DMFT).[37,38] DMFT has been previously used to study the relaxation dynamics of fluids confined in model porous materials,[37–41] for instance in condensation, evaporation, and cavitation processes within the pores, but it has also been used in some membrane studies.[42–44] In this article, we apply DMFT to study the nonequilibrium steady states encountered in permporometry, a technique used in mesoporous membrane characterization.[45–49]

Characterization of mesoporous inorganic membranes has always been a challenge because of their relatively small pore sizes and the fact that they are used as supported thin films. Eyraud et al.[45] made a breakthrough in characterization with the development of permporometry, which probes the pores in a way that reflects their actual contribution to membrane permeation. A permporometry experiment is based on the copermeation of a lighter, noncondensable gas and a heavier, condensable vapor through a porous membrane at different values of the relative partial pressure of the condensable component, $p_r = \frac{y_{\text{condensable}} P}{p_{\text{condensable,sat}}}$. At fixed p_r, the condensable component is expected to fill all pores below a certain size via capillary condensation and effectively block the light gas from permeating through them. A plot of steady-state permeability (or flux) through the membrane as a function of p_r therefore provides qualitative information about the membrane PSD. The main challenge in permporometry is to extract information of a more quantitative nature regarding the PSD. This task requires a model that describes at least three elements: (1) geometry of the pores, (2) adsorption of the condensable component, and (3) transport mechanism of the light gas. Understandably, the first implementations of permporometry[46–49] employed models of minimal complexity. The pores were assumed to be cylindrical (with uniform diameter across the membrane thickness), the Kelvin equation was used to model capillary condensation (with a modification to include the presence of an adsorbed layer, or t-layer, of molecular dimension before full capillary condensation), and the transport mechanism of the light gas was assumed to be Knudsen diffusion through the unblocked pores. There have been surprisingly few attempts to improve these rather minimalist original models or challenge the assumptions therein; indeed, the model used by Higgins et al. in 2006[50] is essentially identical to that proposed 30 years ago. However, weaknesses are starting to emerge. Tsuru et al.[51] found that different condensable species gave different PSDs on the same membrane, especially in the lower pore-size range, which was attributed to effects in t-layer. Recently, Mottern et al.[52] used permporometry to probe for pinhole (macroporous) defects in a supported mesoporous membrane. They found that the light gas diffusion through condensate-filled pores actually contributed to the flux in a significant way, especially in the intermediate regime of p_r where the mesopores were largely filled but the macropores of the support were not. In such cases, transport of the light gas through the liquid-filled mesopores by a solution-diffusion mechanism was appreciable and could easily be misattributed to pinhole defects.

Permporometry represents a very nice application of DMFT because it involves membrane transport in the context of capillary phase transitions. Using a simple slit pore geometry, we demonstrate how DMFT gives a detailed description of the qualitative features of a permporometry experiment. DMFT yields important nanoscale information about the nonequilibrium states including both the density distribution and the flux distribution in the system. The theory includes a full description of the solution thermodynamics and phase behavior for the light/heavy binary mixture and allows for transport of the light component through all regions of the system including the condensed phase regions.

In the next section (Models and Methods Section), we describe the details of our modeling approach, including lattice models of fluid mixtures as well as the essential features of both DFT and DMFT and the detailed implementation of DMFT in the context of permporometry. Results and Discussion Section presents our results for DMFT for a model slit pore membrane and Summary and Conclusions Section gives a summary of our results and conclusions.

Models and Methods

Lattice model and mean field DFT

Our approach starts with a single occupancy, nearest neighbor lattice gas model for a fluid mixture for which the Hamiltonian is written[38,53]

$$H = -\frac{1}{2}\sum_{\mathbf{i}}\sum_{\mathbf{a}}\sum_{\alpha}\sum_{\delta}\epsilon_{\alpha\delta}n_{\mathbf{i}}^{(\alpha)}n_{\mathbf{i}+\mathbf{a}}^{(\delta)}+\sum_{\mathbf{i}}\sum_{\alpha}n_{\mathbf{i}}^{(\alpha)}\phi_{\mathbf{i}}^{(\alpha)} \tag{1}$$

where $\mathbf{i}$ is a set of lattice coordinates, $\mathbf{a}$ denotes the vector to a nearest neighbor site for any site on the lattice, α and δ represent species labels. $\epsilon_{\alpha\delta}$ is the interaction strength between species α and δ, $n_{\mathbf{i}}^{(\alpha)}$ is the occupancy of site $\mathbf{i}$ (0 for empty, 1 for occupied) for component α, and $\phi_{\mathbf{i}}^{(\alpha)}$ represents the external field acting on component α at site $\mathbf{i}$. In this work, the external field is a nearest neighbor attraction of strength $\epsilon_{\alpha W}$ between the wall (pore surface) and molecules of species α occupying sites adjacent to it. In the mean field approximation (mean field DFT or MFT), we can then write the grand free energy of the system as

$$\Omega = kT\sum_{\mathbf{i}}\left[\sum_{\alpha}\rho_{\mathbf{i}}^{(\alpha)}\ln\rho_{\mathbf{i}}^{(\alpha)}+(1-\sum_{\alpha}\rho_{\mathbf{i}}^{(\alpha)})\ln(1-\sum_{\alpha}\rho_{\mathbf{i}}^{(\alpha)})\right]$$
$$-\frac{1}{2}\sum_{\mathbf{i}}\sum_{\mathbf{a}}\sum_{\alpha}\sum_{\delta}\epsilon_{\alpha\delta}\rho_{\mathbf{i}}^{(\alpha)}\rho_{\mathbf{i}+\mathbf{a}}^{(\delta)}+\sum_{\mathbf{i}}\sum_{\alpha}\rho_{\mathbf{i}}^{(\alpha)}(\phi_{\mathbf{i}}^{(\alpha)}-\mu^{(\alpha)}) \tag{2}$$

where $\mu^{(\alpha)}$ is the chemical potential of component α and $\rho_{\mathbf{i}}^{(\alpha)}$ is the average occupancy of site $\mathbf{i}$ by component α. The necessary condition for equilibrium (or metastable equilibrium associated with hysteresis[36]) can be written as

$$\left(\frac{\partial\Omega}{\partial\rho_{\mathbf{i}}^{(\alpha)}}\right)_{\{\mu\},\{\phi\},T} = 0 \ \forall \ \ \alpha,\mathbf{i} \tag{3}$$

where $\{\mu\}$ and $\{\phi\}$ are the fixed set of chemical potentials and external field. Using Eqs. 2 and 3, we find a set of coupled nonlinear equations

$$kT[\ln\rho_{\mathbf{i}}^{(\alpha)}-\ln(1-\sum_{\alpha}\rho_{\mathbf{i}}^{(\alpha)})]-\sum_{\mathbf{a}}\sum_{\delta}\epsilon_{\alpha\delta}\rho_{\mathbf{i}+\mathbf{a}}^{(\delta)}+\phi_{\mathbf{i}}^{(\alpha)}-\mu^{(\alpha)}$$
$$= 0 \ \forall \ \alpha,\mathbf{i} \tag{4}$$

For a system with given geometry and set of chemical potentials and external fields, these equations can be solved by iteration to yield the density distributions for each species and the grand free energy.[38]

For the bulk mixture (no external field, uniform densities, and uniform chemical potentials), we find that

$$Pv_s = \frac{-\Omega}{M} = -kT\ln(1-\sum_{\alpha}\rho_b^{(\alpha)})-\frac{z}{2}\sum_{\alpha}\sum_{\delta}\epsilon_{\alpha\delta}\rho_b^{(\alpha)}\rho_b^{(\delta)} \tag{5}$$

$$\mu^{(\alpha)} = kT[\ln\rho_b^{(\alpha)}-\ln(1-\sum_{\delta}\rho_b^{(\delta)})]-z\sum_{\delta}\epsilon_{\alpha\delta}\rho_b^{(\delta)} \tag{6}$$

where P is the pressure, v_s and M are physical volume equivalent of a lattice site and number of sites in the lattice, respectively, $\rho_b^{(\alpha)}$ is the density of species α in bulk and z is the coordination number of the lattice. We have used these equations to determine the bulk vapor-liquid equilibrium for the mixture, solving the phase equilibrium equations via a combination of Newton–Raphson and pseudo arc length continuation methods.[54]

Dynamic mean field theory

Our implementation of DMFT follows earlier work[37,55] and especially that of Edison and Monson.[38] The time-dependent ensemble average density of a species α at a site $\mathbf{i}$ can be considered by taking the mean of weighted average occupancy of component α for site $\mathbf{i}$ over all possible configurations of the system in terms of occupancies. The weight $P(\{n\},t)$ here is the probability associated with the occurrence of a specific configuration defined by a set of occupation numbers $\{n\}$

$$\rho_{\mathbf{i}}^{(\alpha)} = < n_{\mathbf{i}}^{(\alpha)} > = \sum_{\{n\}} n_{\mathbf{i}}^{(\alpha)}P(\{n\},t) \tag{7}$$

DMFT emerges by making a mean field approximation to the master equation governing Kawasaki dynamics applied to a binary mixture on a lattice gas model. In Kawasaki dynamics, new states are created by molecules hopping to vacant nearest neighbor sites. The evolution of the density species α at any site $\mathbf{i}$ is then described by

$$\frac{\partial\rho_{\mathbf{i}}^{(\alpha)}}{\partial t} = -\sum_{\mathbf{a}}J_{\mathbf{i},\mathbf{i}+\mathbf{a}}^{(\alpha)} \tag{8}$$

where $J_{\mathbf{i},\mathbf{i}+\mathbf{a}}^{(\alpha)}$ is the flux of species α from site $\mathbf{i}$ to one of its nearest neighbor sites $\mathbf{i}+\mathbf{a}$ and in mean field is given by

$$J_{\mathbf{ij}}^{(\alpha)} = w_{\mathbf{ij}}^{(\alpha)}\rho_{\mathbf{i}}^{(\alpha)}(1-\sum_{\delta}\rho_{\mathbf{j}}^{(\delta)})-w_{\mathbf{ji}}^{(\alpha)}\rho_{\mathbf{j}}^{(\alpha)}(1-\sum_{\delta}\rho_{\mathbf{i}}^{(\delta)}) \tag{9}$$

where $w_{\mathbf{ij}}^{(\alpha)}$ is the probability for species α to jump from site $\mathbf{i}$ to $\mathbf{j}$ calculated in accordance with the Metropolis criterion

$$w_{\mathbf{ij}}^{(\alpha)} = w_0^{(\alpha)}\exp\left(-\frac{E_{\mathbf{ij}}^{(\alpha)}}{kT}\right) \tag{10}$$

where $E_{\mathbf{ij}}^{(\alpha)}$ can be identified as the energy change associated with the jump of species α from site $\mathbf{i}$ to $\mathbf{j}$ and $w_0^{(\alpha)}$ is the hopping frequency for species α. In this work, we have assumed w_0 to be the same for all species. The energy change is given by

$$E_{\mathbf{ij}}^{(\alpha)} = \begin{cases} 0, & E_{\mathbf{j}}^{(\alpha)} < E_{\mathbf{i}}^{(\alpha)} \\ E_{\mathbf{j}}^{(\alpha)}-E_{\mathbf{i}}^{(\alpha)}, & E_{\mathbf{j}}^{(\alpha)} > E_{\mathbf{i}}^{(\alpha)} \end{cases} \tag{11}$$

where $E_{\mathbf{i}}^{(\alpha)}$ for a species α at a site $\mathbf{i}$ is the function of densities at the neighboring sites and the external field $\phi_{\mathbf{i}}^{(\alpha)}$

$$E_{\mathbf{i}}^{(\alpha)} = -\sum_{\mathbf{a}}\sum_{\delta}\epsilon_{\alpha\delta}\rho_{\mathbf{i}+\mathbf{a}}^{(\delta)}+\phi_{\mathbf{i}}^{(\alpha)} \tag{12}$$

These expressions are the extension to mixtures of the expressions for pure fluids.[56]

Model system and implementation of DMFT for permporometry

In this initial work, we model a single-slit pore with geometry shown schematically in Figure 1. The system is finite in x and z directions but infinite in y direction. There are bulk fluid zones on the two ends with control volumes for boundary conditions to be specified in the calculations. The control volume 1 (CV1) and control volume 2 (CV2) represent the inlet (feed) and outlet (permeate) conditions for the pore, respectively. Our base case utilizes length (L) of 40 lattice constants, height (H) of 6 lattice constants, and bulk regions that are 10 lattice constants in length including 2 lattice constants of control volume (although only one is necessary). We also vary L and H to study effects of those

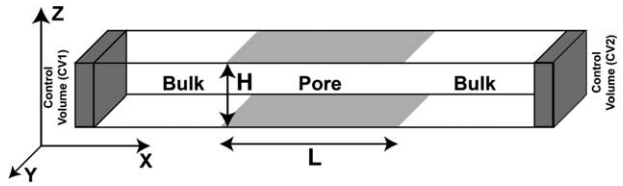

Figure 1. Geometry of the slit pore used to study permporometry.

variables. Interaction parameter values chosen for this study, listed in Table 1, are representative of a typical light/heavy binary mixture that might be employed in permporometry, such as nitrogen/cyclohexane. The light gas is denoted as A while the heavy vapor is denoted as B. The ratio of self interaction parameters ($\epsilon_{BB}/\epsilon_{AA}$) is taken to be 4. This ratio corresponds to the ratio of critical temperatures $T_{c,B}/T_{c,A}$, and 4 is a reasonable value for binary mixtures used in permporometry experiments. The interaction strength between components A and B is taken as the geometric mean of their self interaction parameters, and in each case $\epsilon_{\alpha W} = 3.0\epsilon_{\alpha\alpha}$ to give a fairly strong interaction with the surface relative to the fluid interaction. The thermodynamic variables are defined in dimensionless units using ϵ_{AA} as the base energy unit and v_s as the base volume unit.

$$P^* = \frac{Pv_s}{\epsilon_{AA}} \quad T^* = \frac{kT}{\epsilon_{AA}} \quad \mu^*_\alpha = \frac{\mu_\alpha}{\epsilon_{AA}} \tag{13}$$

We study the system at a temperature $T^* = 4.0$. Note that this T^* is well above the critical temperature of pure A in the context of the mean field lattice model ($T^*_{A,critical} = 1.5$) but is 2/3 of the critical temperature of pure B ($T^*_{B,critical} = 6.0$).

The setup for the permporometry calculations starts with the definition of thermodynamic quantities at the inlet and outlet. We first define the feed (inlet) pressure, P^*_{inlet} and mole fraction of light component $y_{A,inlet}$. Using Eqs. 5 and 6, we can determine the associated bulk densities ($\rho_{A,inlet}$ and $\rho_{B,inlet}$) and bulk chemical potentials ($\mu^*_{A,inlet}$ and $\mu^*_{B,inlet}$) These are taken as conditions for the inlet control volume. A driving force is necessary to simulate the process involved in permporometry. The driving force is provided by setting the chemical potentials at the outlet control volume. The chemical potential of A is set to be slightly lower at the outlet as compared to the inlet, while the chemical potential of B is set to be the same in both locations

$$\mu^*_{A,outlet} = \mu^*_{A,inlet} - \delta\mu^*_A \tag{14}$$

$$\mu^*_{B,outlet} = \mu^*_{B,inlet} \tag{15}$$

The outlet pressure and mole fraction, P^*_{outlet} and $y_{A,outlet}$, are calculated using $\mu^*_{A,outlet}$ and $\mu^*_{B,outlet}$ in Eqs. 5 and 6. The density distribution in the pore and bulk is initialized by solving the static MFT problem for the entire pore at the thermodynamic conditions of inlet control volume. Once the system has been initialized, the thermodynamic quantities at the outlet are changed as described above and the system is allowed to evolve with time, by solving Eq. 8 using Euler's method with a step size of $\omega_0\Delta t = 0.2$, until the it reaches steady state. Then, the flux of component A at the middle cross-section of the pore in the x direction (J^*_A) is computed by summing over the sites at $x = L/2$, while the midpore averaged density is computed using pore sites between $x = L/4$ and $x = 3L/4$. We note that the flux is inherently dimensionless as can be seen in Eq. 8. The density is essentially fractional occupancy and thus dimensionless while the time is in terms of $w_0 t$ which again is dimensionless. The process is repeated for different values of relative pressure of B in the feed, $P_{B,rel} = y_{B,inlet}P^*_{inlet}/P^*_{B_0}$, where $P^*_{B_0}$ is the vapor pressure for pure B; this is done by varying $y_{A,inlet}$. $P^*_{B_0}$ is determined using the static MFT for the bulk fluid.[37] In this setup, we control the inlet pressure, inlet mole fraction of A, and outlet chemical potentials of A and B. This corresponds to an experiment where pressure and component mole fractions are controlled for both sides of the membrane, for example, using a sweep gas on the permeate side. We take the inlet pressure to be $P^* = 0.3001$, which corresponds to a reduced pressure $P^*_{inlet}/P^*_{A,critical} = 1.0359$, so we are slightly above the critical pressure of A (in addition to being well above the critical temperature of A). The operating conditions are specified in Table 2.

Table 1. Interaction Parameters

Component	$\epsilon_{\alpha\alpha}$	$\epsilon_{\alpha W}$
A	1.0	3.0
B	4.0	12.0

Table 2. Operating Conditions

Quantity	Value
P^*_{inlet}	0.3001
T^*	4.0
$y_{A,inlet}$	0.1843–0.9843
$\delta\mu^*_A$	0.005
Reduced Quantities	
$P^*_{inlet}/P^*_{A,critical}$	1.0359
$T^*/T^*_{A,critical}$	2.667
$T^*/T^*_{B,critical}$	0.667

Results and Discussion

We begin this section by presenting the bulk vapor-liquid phase behavior for the binary mixture considered, as calculated in MFT. This is shown in Figure 2a where we have plotted the $p-x-y$ phase diagram at the temperature where our permporometry calculations were made. Vapor-liquid coexistence does not occur across the composition range, which reflects the large difference in critical points for the two components in our model. Also shown on this plot is the locus of inlet conditions for the states studied in the permporometry calculations. The locus of inlet conditions used in the permporometry calculations starts for low values of y_B where the mixture is mostly light gas. As y_B increases, we ultimately approach a dew point, and along that path we should expect the appearance of a condensed phase in the pore, rich in component B, due to the effect of confinement in the pore upon the vapor-liquid equilibrium.

Figure 2b shows equilibrium adsorption/desorption isotherms for the mixture in the slit pore from static MFT with the bulk state following the path of fixed pressure and varying bulk composition (path labeled inlet CV1) shown in Figure 2a. We see that except for low bulk mole fractions of B, y_B, the density of B in the pore is generally much high that of A. The isotherm for B is very similar to that for a pure component system at a similar temperature.[37] This isotherm shows two transition regions. One at low y_B corresponds to the filling of a monolayer near the pore wall. The density of A, which is weakly attracted by the pore walls, remains low

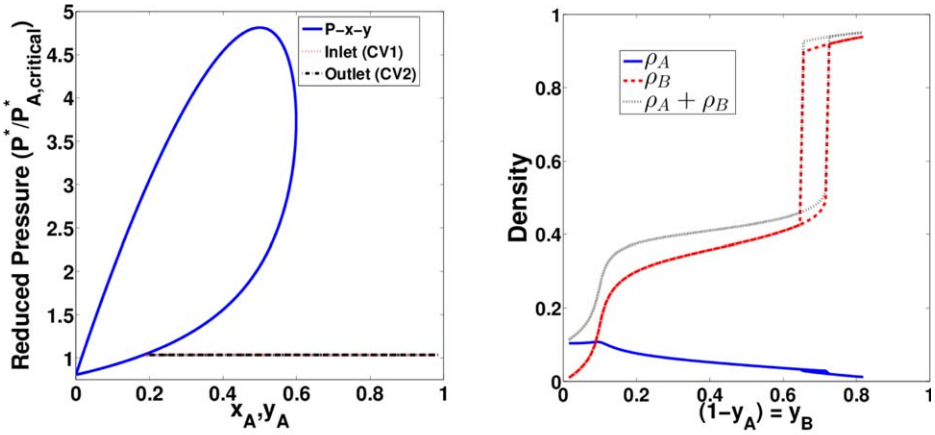

Figure 2. (a) *P-x-y* diagram for binary mixture at $T^* = 4.0$ (blue solid) and the loci of inlet (red dotted) and outlet (black dash-dot) conditions. (b) Midpore averaged density calculated from static MFT for A-B mixture in a slit pore $H = 6$, $L = 40$ at $T^* = 4.0$ and $P^* = 0.3001$.

The blue solid, red dashed, and black dotted curves are for the density of A, density of B, and total density, respectively. [Color figure can be viewed in the online issue, which is available at wileyonlinelibrary.com.]

throughout and is highest when the bulk is mostly A and decreases as A is displaced by the more strongly adsorbed B. The other transition region at higher y_B is associated with condensation of a liquid phase within the pore and is accompanied by hysteresis. The nature of this hysteresis has been discussed in detail in earlier work.[36–38] The states on the liquid branch of the hysteresis loop are equilibrium states while those on the vapor branch are metastable equilibrium states. The metastability on the vapor branch is due to the nucleation barrier to the formation of a liquid bridge. In contrast, on the liquid branch there is no nucleation barrier because the vapor-liquid interface required for evaporation is already present near the pore entrance.

Figure 3a gives a magnification of the low pressure region of the bulk phase diagram from Figure 2a showing the loci of inlet and outlet states for the permporometry calculations. The locus of inlet states is chosen by fixing T and P and then varying y_A. For each outlet state, T and μ_B are fixed at the same values as for the inlet and $\mu_{A,outlet} = \mu_{A,inlet} - \delta\mu_A$. The outlet pressure can then be determined from bulk MFT. The loci of inlet and outlet states are indistinguishable on the scale of the phase diagram plot but the finer scale in Figure 3a shows that the outlet pressure decreases as the outlet mole fraction of A increases. Figure 3b shows a plot of the differences between the inlet and outlet pressures and compositions for the states in the permporometry calculations versus y_A in the feed. The fractional percentage pressure drop relative to the inlet pressure ranges from 0.0294% to 0.1253%.

We now turn to the permporometry results. Figure 4a shows the flux of A through the slit pore vs. the relative partial pressure of B at the inlet. As expected, the flux of A decreases with increasing amount of B in a way that is strongly influenced by the density distributions of the two species. The qualitative behavior seen here is quite similar to that seen experimentally.[47] In parallel with the

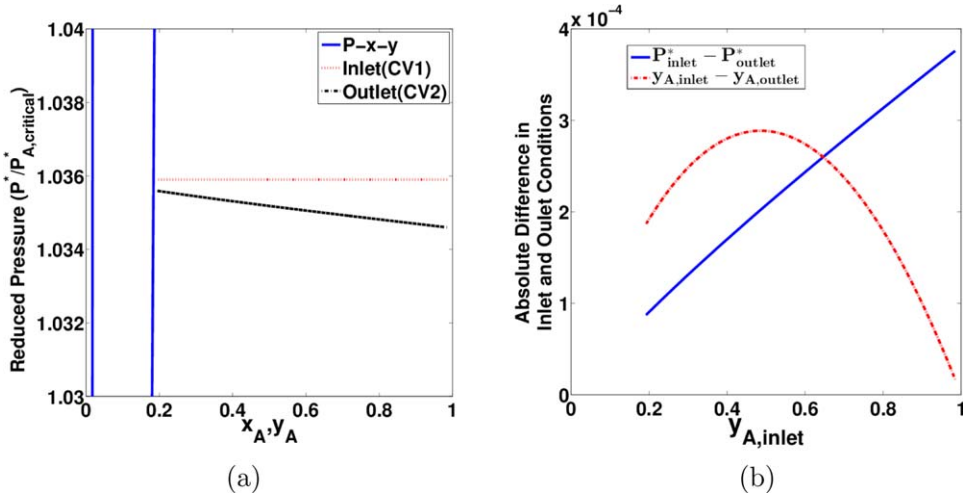

Figure 3. (a) The loci of inlet (red dotted) and outlet (black dot-dashed) conditions with the bulk *P-x-y* (blue solid) for the binary mixture at $T^* = 4.0$. (b) Variation of the difference in inlet and outlet conditions for pressure (blue solid) and mole fraction of A (red dot-dashed) with the inlet mole fraction of A.

[Color figure can be viewed in the online issue, which is available at wileyonlinelibrary.com.]

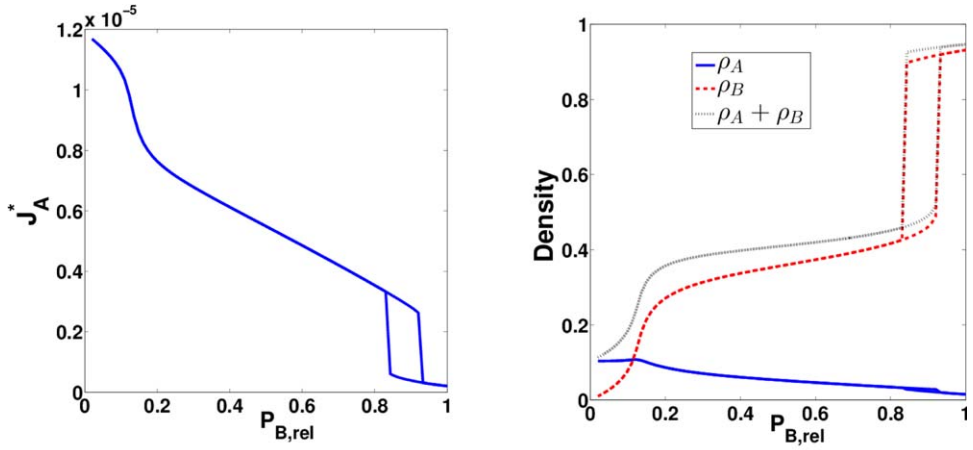

Figure 4. (a) Variation in midpore flux of component A with relative pressure of component B at the inlet. (b) Variation in midpore averaged density with relative pressure of component B at the inlet. Pore length and height are $L = 40$, $H = 6$.

[Color figure can be viewed in the online issue, which is available at wileyonlinelibrary.com.]

adsorption behavior, there are two transition regions in the plot. The first at low relative pressure of B is associated with the formation of dense B-rich layers near the pore walls. The second is associated with the capillary condensation of B-rich liquid in the system, which causes a dramatic drop in the flux of A. The hysteresis seen here parallels that seen in Figure 2b. In fact, when we plot the midpore densities for the steady states obtained in the nonequilibrium calculations, as shown in Figure 4b, we see that they are very similar to those for the equilibrium states shown in Figure 2b. Figure 5 shows visualizations of density distribution of B in selected nonequilibrium steady states. These distributions are very similar to those from static MFT calculations for adsorption in slit pores for a pure component[37] and mixtures.[38] At low relative pressures of B, we see some adsorption on the pore surface followed by the formation of dense monolayers. At higher relative pressures, we see multilayer adsorption and then pore filling. As the relative pressure of B is lowered from the filled state, we see the formation of a meniscus which retreats into the pore. This is followed by evaporation, leaving a state with adsorbed layers on the pore walls. Further decrease in the relative pressure of B leads to states with only slight adsorption on the pore walls. The flux is a product of local density and velocity; the local density dominates flux apart from the initial drop which is a result of the velocity drop (see Supporting Information Figures S1 and S2).

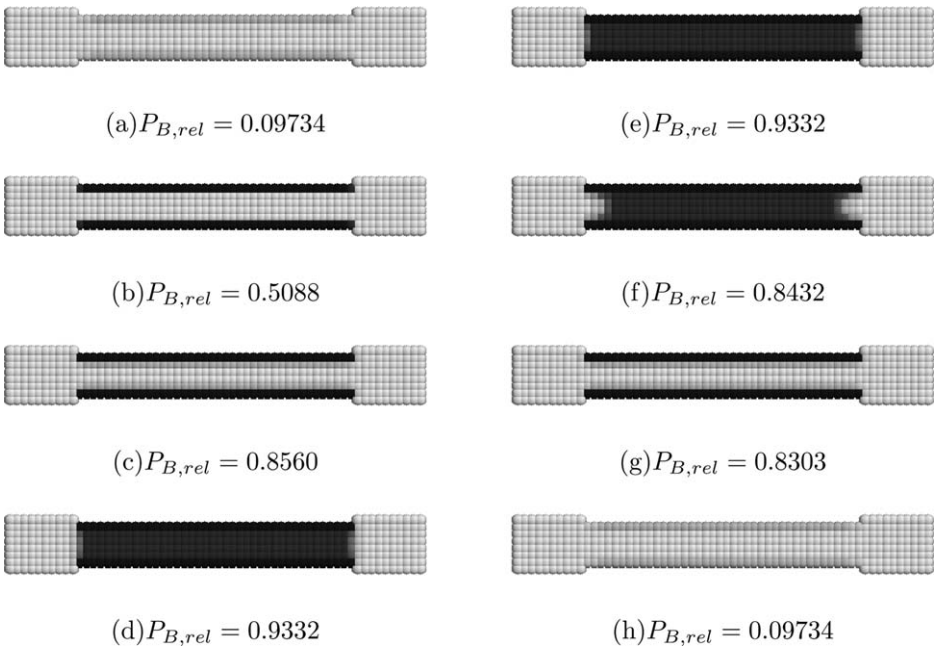

Figure 5. (a)–(d) Visualizations of density of component B during pore filling. (e)–(h) Visualizations of density of component B during pore emptying.

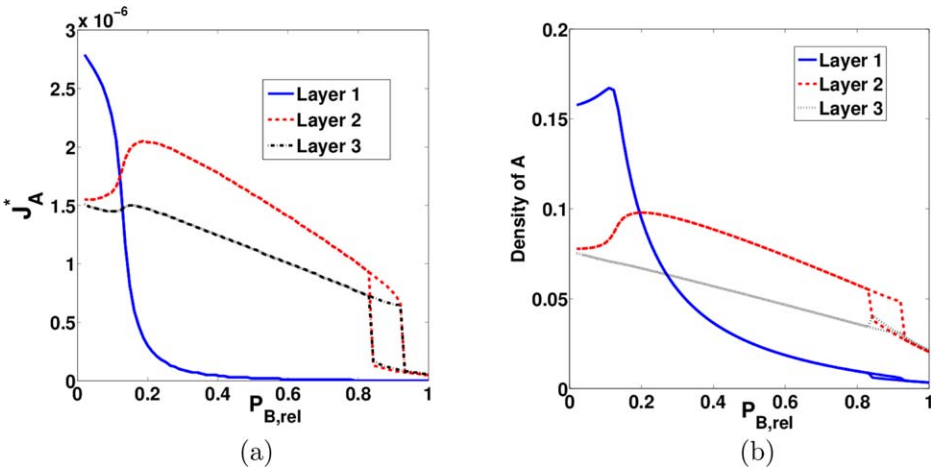

Figure 6. (a) Variation of flux of A with relative pressure of component B at the inlet, for the three unique layers within a slit pore with $H = 6$, $L = 40$. Layer 1 is adjacent to the wall, layer 2 is the next-closest to the wall, and layer 3 is farthest from the wall. (b) Variation of density of A with relative pressure of component B at the inlet, for the three unique layers described in (a).

[Color figure can be viewed in the online issue, which is available at wileyonlinelibrary.com.]

DMFT calculations allow us to probe the flux at an even finer level of detail, as illustrated in Figure 6. Figure 6a shows the contributions to the flux of A from the different layers in the pore while Figure 6b shows the density of A in those layers. For $H = 6$, there are six layers but due to symmetry there are three pairs of layers, with each member of a pair having identical properties. The contribution from the layer nearest the wall is large at low relative pressure of B but drops dramatically as the amount of B in that layer increases. The decrease in flux of A in layer 1 (Figure 6a) occurs in spite of an increase in density of A in layer 1 for low values of relative pressure of B (Figure 6b). This is because as the overall density in the layer 1 is increasing greatly due to the higher density of B which restricts the mobility of A. Interestingly, for higher pressures the largest contribution to the flux comes from layer 2, where the density of A is greatest, rather than layer 3, which is farthest from the walls. The enhanced density of A in layer 2 arises from its attraction to layer 1, which is essentially a dense layer of species B that is adsorbed to the pore wall.

The geometric parameters of the simple slit pore model are the length L and height H. We varied these two parameters independently, away from our base case of $L = 40$ and $H = 6$, and examined the effects on flux. We see from Figure 7a that the position of the hysteresis loop is independent of the length of the pore as it is increased from 40 to 120. This was expected because hysteresis is determined by nucleation of a liquid bridge that is strongly dependent on pore height but not on pore length. The overall magnitude of the flux decreases with increasing pore length, which is again expected because of the increased resistance to transport associated with longer pores. We looked at the variation in

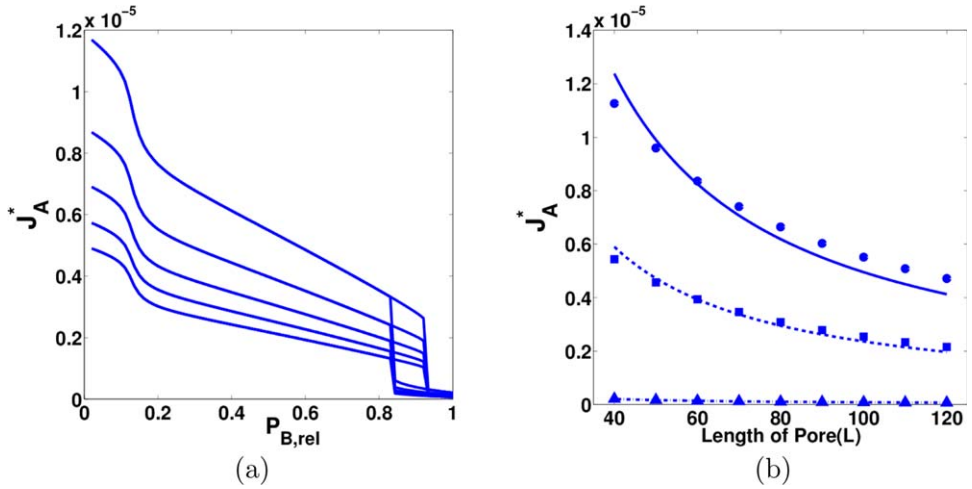

Figure 7. (a) Variation in flux of A with relative pressure of component B at the inlet, for different pore lengths. The plots correspond to pore lengths $L = 40, 60, 80, 100, 120$ in order from top to bottom. (b) Variation in flux of A with length of pore, for three different values of relative pressure of component B at the inlet.

Plots markers (circles, squares, and triangles) correspond to data points from calculations. Plot lines (solid, dashed, and dot dashed) correspond to constant/L fits to data points. The sets of data and fits correspond to $P_{B,rel} = 0.0588, 0.5088, 0.9975$ in order from top to bottom. [Color figure can be viewed in the online issue, which is available at wileyonlinelibrary.com.]

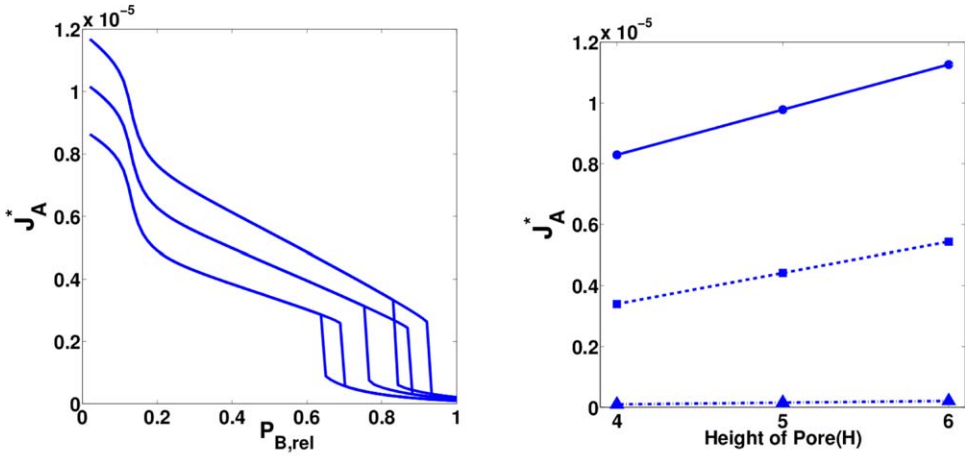

Figure 8. (a) Variation in flux of A with relative pressure of component B at the inlet, for different pore heights. The plots correspond to pore heights $H = 6$, 5, 4 in order from top to bottom. (b) Variation in flux of A with height of pore, for three different values of relative pressure of component B at the inlet.

Plots markers (circles, squares, and triangles) correspond to data points from calculations. Plot lines (solid, dashed, and dot dashed) correspond to constant$_1 \times H$+constant$_2$ fits to data points. The sets of data and fits correspond to $P_{B,rel} = 0.0588$, 0.5088, 0.9975 in order from top to bottom. [Color figure can be viewed in the online issue, which is available at wileyonlinelibrary.com.]

the flux with the length of pore more quantitatively by creating parametric plots at different values of the relative pressure of B, as shown in Figure 7b. The values of relative pressure were chosen to cover three distinct regions in Figure 7a: the initial region before $P_{B,rel} = 0.1$, the region of steady drop between $P_{B,rel} = 0.1$ and 0.8, and the region of lowest flux beyond $P_{B,rel} = 0.9$. Standard continuum models of membrane transport, neglecting any end effects such as concentration polarization or surface barriers, suggest that the flux should scale as $1/L$. The curves in Figure 7b show the best fits to a *constant*/L model, which are quite good in each case.

Pore height strongly affects the relative pressure for capillary condensation, as mentioned above. Flux profiles for $H = 4$, 5, and 6 are shown in Figure 8a. We see that the location of the hysteresis loop moves to higher relative pressure of B with increasing H as expected.[36] Figure 8b shows the flux as a function of pore height for the same three values of relative pressure considered in Figure 7b. At each relative pressure, the dependence of flux on H is fit very well by a linear model with positive slope. We would not always expect such a linear relationship, due to the complexity of the density distributions and transport mechanisms, but such a relationship definitely exists for the cases studied here.

Summary and Conclusions

In this article, we have presented an application of DMFT to permporometry. This theory describes both relaxation dynamics and nonequilibrium steady states in membranes and is fully consistent with a mean field DFT of the thermodynamics. The theory provides additional fundamental basis for the use of permporometry as a characterization tool for membrane pore structure. We have applied the theory to a model membrane consisting of a slit pore in contact with two bulk gas control volumes with different pressures and compositions. As a model mixture, we chose a binary system with a 4:1 ratio of critical temperatures. We determined the phase diagram for this system and then made constant-temperature permporometry calculations along a path of fixed pressure and changing composition (ranging from nearly pure light gas to very near the mixture dew point) at the inlet. The outlet conditions were set so that the chemical potential of the light gas dropped slightly across the pore, while the chemical potential of the heavy vapor was uniform.

The permporometry calculations showed signatures of changes in the species density distributions with relative pressure of the heavy component. We observed the effects of both monolayer formation of at the pore walls and capillary condensation. DMFT also allowed us to study the detailed distribution of flux in the system. We observed that the largest contribution to the light-component flux, over most of the relative pressure range, comes from the layer adjacent to the strongly adsorbed layer of heavy component at the pore wall. This adjacent layer has an enhanced density of the light component due to its energetic affinity for the heavy component. The chemical potential gradients employed in this work were relatively small, and we see that the density distributions and density isotherms are similar to a system with no gradients.

We have shown a relatively simple implementation of DMFT in order to demonstrate the principles involved. However, we emphasize that the approach can be applied to a large variety of membrane structures with both three-dimensional interconnected pore structures as well as systems with hierarchical pore structure. It can of course also be applied to membrane processes other than permporometry. Applications to such systems will be the subject of our ongoing research.

Acknowledgment

This material is based on work supported by the National Science Foundation under Grant No. CBET 1403542.

Literature Cited

1. Burggraaf A, Cot L. *Fundamentals of Inorganic Membrane Science and Technology, Volume 4 of Membrane Science and Technology Series*. Amsterdam, The Netherlands: Elsevier Science B.V., 1996.
2. Kumar P, Guliants V. Periodic mesoporous organic-inorganic hybrid materials: applications in membrane separations and adsorption. *Microporous Mesoporous Mater*. 2010;132(1–2):1–14.
3. Guilants V, Carreon M, Lin Y. Ordered mesoporous and macroporous inorganic films and membranes. *J Membr Sci*. 2004;235(1–2): 53–72.
4. Uhlhorn R, Intveld M, Keizer K, Burggraaf A. Synthesis of ceramic membranes. 1. Synthesis of non-supported and supported gamma-alumina membranes without defects. *J Mater Sci*. 1992;27(2): 527–537.
5. Uhlhorn R, Zaspalis V, Keizer K, Burggraaf A. Synthesis of ceramic membranes. 2. Modification of alumina thin-films - reservoir method. *J Mater Sci*. 1992;27(2):538–552.
6. Yang H, Coombs N, Sokolov I, Ozin G. Free-standing and oriented mesoporous silica films grown at the air-water interface. *Nature*. 1996;381(6583):589–592.
7. Yang H, Coombs N, Dag O, Sokolov I, Ozin G. Free-standing mesoporous silica films; morphogenesis of channel and surface patterns. *J Mater Chem*. 1997;7(9):1755–1761.
8. Brown A, Holt S, Dam T, Trau M, White J. Mesoporous silicate film growth at the air-water interface - direct observation by x-ray reflectivity. *Langmuir*. 1997;13(24):6363–6365.
9. Yang H, Kuperman A, Coombs N, MamicheAfara S, Ozin G. Synthesis of oriented films of mesoporous silica on mica. *Nature*. 1996; 379(6567):703–705.
10. Yang H, Coombs N, Sokolov I, Ozin G. Registered growth of mesoporous silica films on graphite. *J Mater Chem*. 1997;7(7):1285–1290.
11. Akshay I, Trau M, Manne S, Honma I, Yao N, Zhou L, Fenter P, Eisenberger PM, Gruner SM. Biomimetic pathways for assembling inorganic thin films. *Science*. 1996;273(5277):892–898.
12. Ogawa M. Formation of novel oriented transparent films of layered silica-surfactant nanocomposites. *J Am Chem Soc*. 1994;116(17): 7941–7942.
13. Bruggen BVD, Vandecasteele C, Gestel TV, Doyen W, Leysen R. A review of pressure-driven membrane processes in wastewater treatment and drinking water production. *Environ Prog*. 2003;22(1): 46–56.
14. Girard B, Fukumoto LR. Membrane processing of fruit juices and beverages: a review. *Crit Rev Food Sci Nutr*. 2000;40(2):91–157.
15. Hsieh HP. *Inorganic Membranes for Separation and Reaction*. Amsterdam: Elsevier Sceince B.V., 1996.
16. Chew TL, Ahmad A, Bhatia S. Ordered mesoporous silica (OMS) as an adsorbent and membrane for separation of carbon dioxide (CO_2). *Adv Colloid Interface Sci*. 2010;153(1–2):43–57.
17. Sakamoto Y, Nagata K, Yogo K, Yamada K. Preparation and CO_2 separation properties of amine-modified mesoporous silica membranes. *Microporous Mesoporous Mater*. 2007;101(1–2):303–311.
18. Kumar P, Ida J, Kim S, Guliants V, Lin J. Ordered mesoporous membranes: effects of support and surfactant removal conditions on membrane quality. *J Membr Sci*. 2006;279(1–2):539–547.
19. Busca G, Berardinelli S, Resini C, Arrighi L. Technologies for the removal of phenol from fluid streams: a short review of recent developments. *J Hazard Mater*. 2008;160(2–3):265–288.
20. Huang P, Xu N, Shi J, Lin Y. Recovery of volatile organic solvent compounds from air by ceramic membranes. *Ind Eng Chem Res*. 1997;36(9):3815–3820.
21. Park DH, Nishiyama N, Egashira Y, Ueyama K. Enhancement of hydrothermal stability and hydrophobicity of a silica MCM-48 membrane by silylation. *Ind Eng Chem Res*. 2001;40(26):6105–6110.
22. Javaid A, Hughey M, Varutbangkul V, Ford D. Solubility-based gas separation with oligomer-modified inorganic membranes. *J Membr Sci*. 2001;187(1–2):141–150.
23. Javaid A, Ford DM. Solubility-based gas separation with oligomer-modified inorganic membranes - part II. Mixed gas permeation of 5 nm alumina membranes modified with octadecyltrichlorosilane. *J Membr Sci*. 2003;215(1–2):157–168.
24. Javaid A, Krapchetov DA, Ford D. Solubility-based gas separation with oligomer-modified inorganic membranes - part III. Effects of synthesis conditions. *J Membr Sci*. 2005;246(2):181–191.
25. Javaid A, Gonzalez S, Simanek E, Ford D. Nanocomposite membranes of chemisorbed and physisorbed molecules on porous alumina for environmentally important separations. *J Membr Sci*. 2006; 275(1–2):255–260.
26. Yoo S, Lunn JD, Gonzalez S, Ristich JA, Simanek EE, Shantz DF. Engineering nanospaces: OMS/dendrimer hybrids possessing controllable chemistry and porosity. *Chem Mater*. 2006;18(13):2935–2942.
27. Yoo S, Yeu S, Sherman R, Simanek E, Shantz D, Ford D. Reverse-selective membranes formed by dendrimers on mesoporous ceramic supports. *J Membr Sci*. 2009;334(1–2):16–22.
28. Williams J, Seaton N, Duren T. Influence of surface groups on the diffusion of gases in MCM-41: a molecular dynamics study. *J Phys Chem C*. 2011;115(21):10651–10660.
29. Frentrup H, Avendaño C, Horsch M, Salih A, Müller EA. Transport diffusivities of fluids in nanopores by non-equilibrium molecular dynamics simulation. *Mol Simul*. 2012;38(7):540–553.
30. Huang C, Choi PYK, Nandakumar K, Kostiuk LW. Comparative study between continuum and atomistic approaches of liquid flow through a finite length cylindrical nanopore. *J Chem Phys*. 2007; 126(22):224702.
31. Pohl PI, Heffelfinger GS. Massively parallel molecular dynamics simulation of gas permeation across porous silica membranes. *J Membr Sci*. 1999;155(1):1–7.
32. Cracknell RF, Nicholson D, Quirke N. Direct molecular dynamics simulation of flow down a chemical potential gradient in a slit-shaped micropore. *Phys Rev Lett*. 1995;74:2463–2466.
33. Evans R. Fluids adsorbed in narrow pores: phase equilibria and structure. *J Phys: Condens Matter*. 1990;2(46):8989.
34. Gelb LD, Gubbins KE, Radhakrishnan R, Sliwinska-Bartkowiak M. Phase separation in confined systems. *Rep Prog Phys*. 1999;62(12): 1573–1659.
35. Neimark A, Ravikovitch P, Vishnyakov A. Bridging scales from molecular simulations to classical thermodynamics: density functional theory of capillary condensation in nanopores. *J Phys: Condens Matter*. 2003;15(3):347–365.
36. Monson P. Understanding adsorption/desorption hysteresis for fluids in mesoporous materials using simple molecular models and classical density functional theory. *Microporous Mesoporous Mater*. 2012; 160:47–66.
37. Monson PA. Mean field kinetic theory for a lattice gas model of fluids confined in porous materials. *J Chem Phys*. 2008;128(8):084701.
38. Edison JR, Monson PA. Dynamic mean field theory for lattice gas models of fluid mixtures confined in mesoporous materials. *Langmuir*. 2013;29(45):13808–13820.
39. Edison JR, Monson PA. Dynamics of capillary condensation in lattice gas models of confined fluids: a comparison of dynamic mean field theory with dynamic Monte Carlo simulations. *J Chem Phys*. 2013;138(23):234709.
40. Kierlik E, Leoni F, Rosinberg ML, Tarjus G. Spontaneous imbibition in a slit pore: a lattice-gas dynamic mean field study. *Mol Phys*. 2011;109:1143–1157.
41. Leoni F, Kierlik E, Rosinberg ML, Tarjus G. Spontaneous imbibition in disordered porous solids: a theoretical study of helium in silica aerogels. *Langmuir*. 2011;27(13):8160–8170.
42. Matuszak D, Aranovich GL, Donohue MD. Modeling fluid diffusion using the lattice density functional theory approach: counterdiffusion in an external field. *Phys Chem Chem Phys*. 2006;8(14):1663–1674.
43. Matuszak D, Aranovich GL, Donohue MD. Single-component permeation maximum with respect to temperature: a lattice density functional theory study. *Ind Eng Chem Res*. 2006;45(16):5501–5511.
44. Ten Bosch A. Analytical theory for permeation of condensable gases in a nanopore. *J Membr Sci*. 2008;323(2):271–277.
45. Eyraud C, Betemps M, Quinson J, Chatelut F, Brun M, Rasneur B. Determination of the pore-size distribution of an ultrafilter by - gas-liquid permporometry measurement - comparison between flow porometry and condensate equilibrium porometry. *Bull Soc Chim Fr I*. 1984;1(9–10):237–244.
46. Cuperus FP, Smolders CA. Characterization of UF membranes - membrane-characteristics and characterization techniques. *Adv Colloid Interface Sci*. 1991;34:135–173.
47. Cuperus F, Bargeman D, Smolders C. Permporometry - the determination of the size distribution of active pores in UF membranes. *J Membr Sci*. 1992;71(1–2):57–67.
48. Cao G, Meijerink J, Brinkman H, Burggraaf A. Permporometry study on the size distribution of active pores in porous ceramic membranes. *J Membr Sci*. 1993;83(2):221–235.
49. Huang P, Xu N, Shi J, Lin Y. Characterization of asymmetric ceramic membranes by modified permporometry. *J Membr Sci*. 1996;116(2):301–305.

50. Higgins S, Kennard R, Hill N, DiCarlo J, DeSisto W. Preparation and characterization of non-ionic block co-polymer templated mesoporous silica membranes. *J Membr Sci*. 2006;279(1–2):669–674.
51. Tsuru T, Hino T, Yoshioka T, Asaeda M. Permporometry characterization of microporous ceramic membranes. *J Membr Sci*. 2001; 186(2):257–265.
52. Mottern ML, Shqau K, Zalar F, Verweij H. Permeation porometry: effect of probe diffusion in the condensate. *J Membr Sci*. 2008; 313(1–2):2–8.
53. Woywod D, Schoen M. Phase behavior of confined symmetric binary mixtures. *Phys Rev E*. 2003;67(2):026122.
54. Keller HB. Numerical solution of bifurcation and nonlinear eigenvalue problems. In Rabinowitz PH, editor. *Applications of Bifurcation Theory*. New York: Academic Press, 1977:359–384.
55. Gouyet JF, Plapp M, Dieterich W, Maass P. Description of far-from-equilibrium processes by mean-field lattice gas models. *Adv Phys*. 2003;52(6):523–638.
56. Matuszak D, Aranovich GL, Donohue MD. Lattice density functional theory of molecular diffusion. *J Chem Phys*. 2004;121(1):426–435.

Manuscript received Jan. 12, 2015, and revision received Apr. 15, 2015.